

Grain Boundary Assisted Crevice Corrosion in CoCrMo Alloys

Emily E. Hoffman,* Alex Lin,* Yifeng Liao,** and Laurence D. Marks‡*

ABSTRACT

Cobalt chromium molybdenum alloys have been extensively used for biomedical implants, but are susceptible to grain boundary corrosion resulting from local chromium depletion, which is called sensitization. This work extended the understanding of chromium depleted zones in CoCrMo alloys and their role in corrosion to the nanoscale. Selected boundaries were analyzed from the millimeter to the nanometer scale in order to link the chemical composition and crystallographic structure to the observed local corrosion properties. The shape and severity of grain boundary corrosion crevices were measured, linked with the coincidence site lattice geometry. Additionally, direct high-resolution energy dispersive x-ray spectroscopy maps of chromium depleted zones at the grain boundaries were measured to completely characterize the grain boundary properties. Chromium depleted zones were found in 100% of corroded grain boundaries, yet were too small to follow classical models of sensitization. Nanoscale regions of chromium depletion were found to have significant effects on corrosion initiation. This led to a grain boundary crevice corrosion model connecting the chemical composition with electrochemical driving forces that control crevice corrosion propagation. The conclusions and model presented can be used to better develop processing techniques for CoCrMo and other alloys.

KEY WORDS: biocorrosion, chromium, cobalt, grain segregation, microstructure, sensitization, transmission electron microscopy

Submitted for publication: April 7, 2016. Revised and accepted: June 27, 2016. Preprint available online: June 28, 2016, <http://dx.doi.org/10.5006/2108>.

* Corresponding author. E-mail: L-marks@northwestern.edu.

‡ Department of Materials Science and Engineering, Northwestern University, 2220 Campus Drive, Cook Hall Rm 2036, Evanston, IL 60208.

** Current address: Dow Corning Corporation, Midland, MI.

INTRODUCTION

As the “baby boom” generation ages and as patients continue to live longer and have more active lives, the demand for hip replacements has risen. Injury and osteoarthritis often result in a patient’s need for a hip or knee replacement. For total hip arthroplasties, the number of implants in the United States is expected to grow from 2005 by at least 174% to 572,000 implants by 2030.¹⁻²

Beginning in the 1970s, cobalt chromium molybdenum (CoCrMo) alloys have been approved as implantable biomedical materials for hip replacements.³ Advantages of this metal alloy include the good bulk mechanical properties, which can be predictably modified by various processing techniques such as casting, annealing, hot forging, and cold working.⁴⁻⁸ Of the different articulating joint interfaces available for hip implants, metal-on-metal (MoM) is known to have one of the lowest wear rates compared to systems with the polymer polyethylene.^{3,9} The MoM implants, however, have generated serious clinical concerns as a result of metal wear products being released into the surrounding tissues.¹⁰ One of the major degradation processes that affect all metallic implants in vivo is corrosion.¹¹⁻¹³ While CoCrMo alloys have good tribological properties and are especially corrosion resistant resulting from the formation of a passive oxide film, cobalt and chromium cations and nanoparticles have been detected in patients with implants.^{7,14-17} Complications observed clinically as a result of corroding CoCrMo alloys include metal hypersensitivity, metallosis (metallic staining of the surrounding tissue),

excessive periprosthetic fibrosis, and adverse local tissue responses (which can include extensive necrosis of periprosthetic tissues), all of which have contributed to CoCrMo falling out of favor at present. While there are developments with new alloys and increasing use of materials other than CoCrMo alloys such as titanium for the primary mechanical supports in implants, many CoCrMo alloys still continue to be used and currently exist in millions of patients worldwide. It is medically unreasonable (and detrimental to a patient's health) to remove an implant that is not displaying any signs of unfavorable physiological reactions. Considering the millions of MoM hip replacements in use worldwide, a better understanding of the fundamental processes of grain boundary corrosion in these alloys is needed. Beyond the medical applications, understanding corrosion of CoCrMo alloys is important for naval and industrial applications.

In all forms of CoCrMo alloys, with variations in carbon concentrations, precipitates, and microstructures, the dominant corrosion protection comes from the formation of a chromium oxide thin film at the surface. In many cases of extended corrosion, there is not a constant mass loss per unit area, rather, preferential mass loss at grain boundaries, carbide phases, or defects. A particularly important contribution to the *in vivo* corrosion is the more rapid mass loss near the intersection of grain boundaries of the metallic alloy and the protective oxide. This is often called "grain boundary sensitization" and the alloys that easily corrode after certain heat treatments are described as sensitized.¹⁸⁻²⁰ For alloys that include chromium, the most common explanation of local sensitization is a local reduction in the chromium concentration.^{7,18,21-22} Failed implants have been explanted and studied for intergranular corrosion. The attack can occur on all modular parts of the implant, and the degradation is the result of both electrochemical dissolution and physical wear.^{11,19,23} Scanning electron micrographs (SEMs) proved specific attacks at grain boundaries and carbide phases, often penetrating deep into the microstructure and causing grain fallout.²³ In CoCrMo alloys, these particles and ions generated from the grain boundary attack play a pathogenic role in osteolysis and aseptic loosening, which can lead to the need for a revision surgery.²³⁻²⁴ As will be discussed in more detail later, the majority of the evidence for boundary attack is based upon rather large-scale segregation at the 0.1 μm to 10 μm scale, which leaves open the question of what takes place with much finer-scale segregation at the nanoscale.

In this work, the nanoscale structure and segregation in CoCrMo alloys that has often been overlooked in microscale carbide precipitate analysis is investigated. Through analysis of carbide phases and chemical compositions at grain boundaries, grain boundary properties are connected to the occurrence of local grain boundary corrosion attack.

High-resolution characterization techniques, including transmission electron microscopy (TEM) and energy dispersive x-ray spectroscopy (EDS), show the chemical segregation that occurs at the nanoscale. By modeling the grain boundary energies, it was possible to predict the grain boundary corrosion and obtain insights into developing the next generation of CoCrMo alloys.

The structure of this paper is as follows. First, a background on sensitization is presented to clarify terms used in literature and establish the field as relevant to CoCrMo alloys. Next, the various techniques used to characterize the CoCrMo corroded alloy are described and the TEM images, composition data, and summary statistics are presented. Based upon the EDS quantitative composition data, a model, grain boundary assisted crevice corrosion (GACC), is presented, which combines the energy of coincidence site lattice and sensitized grains to explain the shape of crevice corrosion observed at the grain boundaries. Finally, this paper is concluded by connecting these results to future designs of CoCrMo alloys for biomedical or other uses.

GRAIN BOUNDARY SENSITIZATION

A brief overview of grain boundary sensitization as currently understood in the literature is provided as a prelude to the nanoscale results described later.

The term sensitization, as currently used in the literature, is the change in an alloy's corrosion properties as result of heat treatments.^{11-12,20,25-28} For a variety of chromium-containing alloys and others such as magnesium-containing alloys, sensitization is widely used to describe the basic cause of intergranular corrosion (IGC) and intergranular stress corrosion cracking (IGSCC).²⁹⁻³⁶ The most general use of sensitization refers to a local reduction of the concentration of a protective alloying element. While this may not be the only possible reason for preferential corrosion at grain boundaries, it is the most commonly invoked source. For the specific case of CoCrMo alloys herein, the term sensitization will be used as it is applied to other chromium-containing alloys, with "grain boundary sensitization" referring to the formation of chromium depleted zones (CDZ) adjacent to grain boundaries resulting from the presence of chromium-rich carbides.^{18,37} For chromium-containing steel, nickel, and cobalt alloys, it is known that during alloy processing, annealing, and heat treatments, chromium-rich carbides precipitate primarily at the grain boundaries, and the growth of these carbides leads to depleted regions in the immediate surroundings.^{18,38-39} The understanding of corrosion causes and prevention has motivated over 90,000 published studies, as avoiding grain boundary sensitization is critical for high performance alloys.

This chemical segregation along the grain boundary has been most commonly studied in stainless

steels, with fewer studies focusing on nickel or cobalt alloys. Often for stainless steels, the goal is to develop maps of carbon content, chromium content, alloying time, and alloying temperature and thereby direct engineers to safe, corrosion resistant alloys.^{29,40-42} Various heat treatments have been studied to reduce the volume fraction of chromium carbides, attempting to ensure that chromium is even throughout the matrix, and promote the formation of protective oxide in order to control the corrosion resistance of a metal.^{25-26,32} In general, the samples were analyzed for corrosion resistance by a range of methods generally at the mesoscale, with the target of comparing several different alloys and microstructures and their relative corrosion rates.

The effects of sensitization were often demonstrated through accelerated corrosion testing, and then measured through electrochemical tests, including potentiodynamic tests, potentiostatic tests, and electrochemical potentiokinetic reactivation tests.^{18,38,43-46} The term “degree of sensitization” (DoS) is widely used and loosely defined, and it usually refers to the intensity and size of the CDZ at the grain boundaries.^{22,30,39,47-48} The DoS was usually inferred from electrochemical tests or fit using a model, rarely directly measured. The chromium depleted zones were linked to corrosion, as they were reported to leave the alloy unable to form the necessary Cr_2O_3 protective oxide in that region.^{7,20,25-26,49-51}

It is widely considered in the literature that carbides play a major role in grain boundary sensitization, as the formation of chromium carbides at the grain boundary leaves nearby zones of chromium depletion.^{28,43,47-48,52-53} This was based upon observations at the microscale, often observing materials that form extensive carbide phases along an entire boundary.^{28,38,43} As shown in Figure 1, the carbide coverage can be a complete phase along a grain boundary as in (a), can be micrometer scale precipitates as in (b), or can have unnoticed nanoscale precipitates as in (c). In CoCrMo alloys, only carbides such as those in Figures 1(a) and (b) have been observed to date with light or scanning electron microscopy. Often

the presence of carbides was enough to conclude that a CDZ was present, and it was assumed that grain boundary sensitization was the cause of the corrosion.^{20,26,44} Some chemical profiles have indicated the composition of the carbides to be chromium carbide (Cr_{23}C_6) and that in CoCrMo alloys some carbides were molybdenum carbides (Mo_6C).^{22,25,52,54} Even including stainless steel, sensitization has only been studied down to hundreds of nanometers. It is unknown if carbides and CDZs of smaller length scales affect corrosion properties.

In addition to chemical composition of carbides and the CDZ, the geometric organization of a grain boundary lattice can also affect carbide formation and therefore sensitization.^{31,42-43,55} Grain boundary orientation is typically quantified using the coincidence site lattice (CSL) approach, where grain boundaries are classified as having a repeating match along the boundary (described by a Σ value). Boundaries with low CSL have been found to inhibit the depletion of soluble chromium in the vicinity of the grain boundary and therefore resist the formation of carbides and CDZs, leading to improved corrosion resistance.^{43,56-57} For example, in nickel, grain boundaries with $\Sigma < 29$ were considered to have “special” properties.^{21,56} In heat treated CoCrMo alloys, grain boundaries below $\Sigma 9$ were immune to corrosion.⁵⁷ Additionally, boundaries with intrinsic dislocations along the boundaries have been demonstrated to act as sinks for solutes, i.e., forming chromium carbides. Intergranular boundary defects can act as preferential sites for breakdown of the protective oxide film, and with increasing chromium depletion, the barrier to initiate corrosion at these sites is reduced.²¹ The goal of understanding the role of CSL in corrosion is to enable engineering of the grain boundary orientations to favor boundaries that resist corrosion in order to improve the bulk corrosion resistance.^{55,58-61}

Models have been developed to predict the extent of sensitization, focusing primarily on stainless steels and on the length and temperature of the heat treatment.^{22,30,47-48} Proposed models have used three

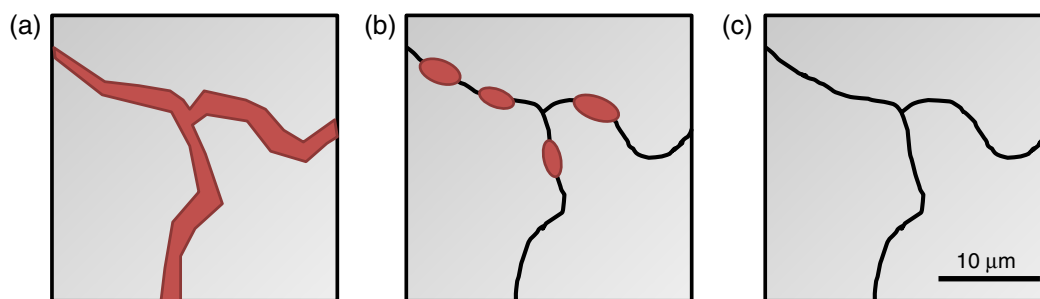


FIGURE 1. Carbide presence at a grain boundary may take the form of (a) a complete network along the grain boundary, (b) micrometer scale precipitates along some parts of the boundary, or (c) nanoscale precipitates unable to be seen at the micrometer scale.

parameters to characterize CDZ: coverage, width, and depth.^{38,43} Coverage is the proportion of the grain boundary length covered by CDZs. Width is the depleted zone perpendicular to the grain boundary. Depth is the minimum level of chromium in the depleted zone. Additionally, previous work has attempted to link the width of sensitization to the width of the crevice corrosion observed, but it was always shown that the crevice is much larger than the sensitized region in the model.^{30,38} Width was always found to be narrower than the electrochemically corroded area and not a predictor of corrosion intensity.

The stainless steel models have used thermodynamic calculations to analyze the equilibrium concentration of chromium in the matrix at the carbide/matrix interface.^{28,30,62} The quantitative composition of sensitization reported for stainless steel often cites Stawstrom and Hillert, where sensitization was said to occur at less than 13 at% Cr for a width greater than 20 nm at the grain boundary.³⁰ It was reported in stainless steels that when the level of chromium in the depletion falls below 12 at% to 13 at%, the passive film over the depleted region becomes easily breached to initiate corrosion and degradation,^{28,30} leading to most stainless steel models having a composition around 19 at% Cr and assuming sensitization around 13 at% Cr.^{48,63-65} These models for sensitization have not been expanded to cobalt alloys, and involved precipitates on a scale of 100 s of nanometers to micrometers, without consideration of nanoscale precipitates.

Much less is known about CoCrMo alloys compared to stainless steels. In steels, some studies have done EDS line scans on the range of 100s of nanometers to directly measure CDZ, and then linked the composition data to predictive models. These models, however, were often for micrometer-sized carbides with large CDZs. In CoCrMo alloys, the scale of investigation has also focused on micrometer-sized carbides and extensive carbide phases along an entire boundary.^{20,49} The majority of the sensitization conclusions were made after electrochemical measurements were taken. Previous studies have at most taken point compositions or coarse micrometer scale line scans across carbides and CDZs, often presenting only one composition profile scan.^{25-26,52} Some studies have characterized the nanoscale compositions of various carbides,⁶⁶ but not in relation to heat treatment or corrosion, and there are studies which looked at CSL, heat treatment, and corrosion, but did not consider composition.^{21,57,67}

To summarize this section, grain boundary sensitization resulting from mesoscale segregation is fairly well understood in many steels, but less so in CoCrMo alloys. The extent that grain boundary sensitization concepts at this large scale can or should be used for segregation at the nanoscale is a rather open question.

METHODS

CoCrMo Alloy

The CoCrMo alloy used was a high-carbon (HC) wrought alloy from ATI Allvac with a composition corresponding to ASTM F1537-08.⁶⁸ The composition is given in Table 1. The samples' heat treatments, microstructure, and electrochemical treatment have been described in previous work by Panigrahi, et al.⁵⁷ For this study, a HC wrought pin annealed at 1,230°C for 24 h was used, as this anneal was most successful in reducing overall corrosion rate and localizing corrosion to grain boundaries.⁵⁷ After the anneal, the sample was quenched in water.

Electrochemical Corrosion Testing

The sample of CoCrMo alloy used in this work was previously studied by Panigrahi, et al.,⁵⁷ and the sample's electrochemical corrosion testing and properties are described in detail in the previous publication. To summarize, the samples were mechanically polished immediately prior to electrochemical corrosion testing. The sample was then corroded in a custom four-chamber electrochemical cell that served as a working electrode, along with a graphite counter electrode and a saturated calomel electrode reference electrode. The corrosion cell was filled with 10 mL of bovine calf serum (BCS) with a protein content of 30 g/L, buffered to a basic pH of 7.4, and placed in a hot water bath maintained at 37°C to mimic physiological conditions. Buffering a biological solution typically involves adding phosphate-buffered saline, NaCl, or NaOH.

A standard protocol was used for the electrochemical tests. The tests began with a potentiostatic test to standardize the surface, then an electrochemical impedance spectroscopy test was conducted. A potentiodynamic (cyclical polarization) test was performed to corrode the sample and measure the current at each applied potential. The samples were anodically polarized from -0.8 V to 1.8 V at a scan rate of 2 mV/s and then reversed back down to -0.8 V at the same rate. Using the corrosion current from the results of Panigrahi, et al., and Faraday's equation, the dissolution rate was calculated to be 2.98×10^{-3} mm/y. Based on the previous study, congruent dissolution is assumed.

Electron Backscatter Diffraction

Electron backscatter diffraction (EBSD) methods were used to create orientational image maps (OIMs) of

TABLE 1
Composition of the High-Carbon CoCrMo Alloy

at%	Co	Cr	Mo	C	Mn	Si	Ni	Fe
Balance	30.3	3.6	1.14	0.73	1.34	0.17	0.14	

selected regions of the annealed CoCrMo sample. An FEI Quanta ESEM[†] with an EBSD detector was used to acquire and index diffraction patterns for multiple 2D arrays on the sample surface. An accelerating voltage of 20 kV and a step size of 0.5 μm were used, as these conditions supplied enough resolution and signal to map the CSLs of relevant grain boundaries. Orientational indexing from the Kikuchi patterns was performed using the commercially available Oxford AZtec[†] EBSD processing software, assuming a single face-centered cubic (fcc)-Co matrix phase. Using the Oxford Tango[†] software, noise reduction was performed to minimize the role of the roughness of the corroded surface, and misorientation matrices for each grain boundary were calculated from the Euler angles. Each grain boundary was mapped as a high-angle or a low-angle grain boundary. For the high-angle boundaries ($>15^\circ$ misorientation angle), the Brandon Criterion⁶⁹ was used to determine the reciprocal CSL density Σ based on the geometric 3D misorientation with lattice coincidence for fcc crystals.

White Light Interferometry

A Bruker Contour GT-K[†] 3D optical microscope equipped with a Mirau interferometer objective lens was used to quantitatively measure the topography of the corroded grain boundaries. The white light interferometer had a lateral resolution limited by the wavelength of light and a finer z-axis resolution limited by the sensitivity of the light intensity detector.⁷⁰ This technique was used to measure the width of corroded grain boundaries and depth of corroded regions with respect to the surrounding surface.

A magnification of 40 \times was used to capture the profile of the corroded surface in a 2D projection of approximately 250 μm in length and 300 μm in width. In total, 25 grain boundaries, 13 CSL boundaries, and 12 non-CSL boundaries were characterized for their depth and width. For each individual grain boundary, 15 to 20 depth and width measurements were collected along the boundary. On average, a single depth measurement was acquired per 0.5 μm to 1.0 μm along the boundary. The width of the corroded boundary was acquired by measuring the distance between the two edges of the corroded crevice at the boundary. The mean of the depth and width measurements were computed, along with the range to a 95% confidence level.

Focused Ion Beam

An FEI NanoLab[†] dual-beam focused ion beam (FIB) system was used to prepare lamellar TEM samples from the annealed CoCrMo alloy. The FIB used a scanning electron imaging beam operated at 5 kV and 1.4 nA and a focused ion milling beam orientated at 52° to the electron beam operating at 30 kV from 9.2 nA

to 48 nA. Specific grain boundaries were identified from the OIM data and a cross section of the boundary was made into a ~ 100 nm thick, electron-transparent TEM sample for further analysis. The lamellar sample created was a cross section of the grain boundary, approximately 5 μm on either side of the boundary and 5 μm deep below the bulk surface (see Figure 2). Twenty-two grain boundary FIB samples were prepared. Twelve corroded boundaries and 10 immune boundaries were prepared and imaged, including 10 non-CSL corroded grain boundaries, 2 CSL corroded boundaries, 5 non-CSL immune boundaries, and 5 CSL immune boundaries.

FIB was also used to prepare grain boundary samples for use in local-electrode atom-probe (LEAP) tomography. The samples were prepared by the lift out process and sharpened by milling, with special attention paid to orienting a grain boundary through the area of the sharpened tip.⁷¹ A platinum protective layer and a final milling at 5 kV were used to prevent ion implantation in the region of interest.

Transmission Electron Microscopy and Energy Dispersive X-Ray Spectroscopy

TEM was performed to analyze the structure and composition of the grain boundary FIB samples to compare between corroded and immune boundaries. A JEOL 2100[†] TEM was used for bright field, dark field, diffraction, and high-resolution imaging, and EDS chemical analysis. The EDS on the TEM had a 1 nm probe size, with most analysis confined to line scans for minimum noise, and processed through Inca[†] software.

TEM was also performed on a JEOL ARM200CF[†] with a windowless EDS detector for high-resolution EDS mapping of four selected grain boundary FIB samples. The aberration corrected microscope provided an EDS analysis probe size of approximately 0.13 nm. For carbide composition quantification, measurements were taken from two to four carbides per boundary for each sample. The EDS quantification spectra were taken from three regions of each carbide—the carbide, the CDZ, and the matrix—indicated in the maps. The maps were collected and analyzed using the Oxford AZtec[†] TEM software.

Atom Probe Tomography

Atom probe tomography (APT) analysis was performed using a LEAP tomograph manufactured by Imago Scientific Instruments. The analysis was formed at a specimen temperature of 25 K, a pulse repetition frequency of 500 kHz, a laser energy of 40 pJ, and a detection rate of 0.01%. Reconstruction was done by means of IVAS 3.6.8[†] using SEM profiles of the tips for the shape reference. Line scans were generated using 2D regions of interest and normalized to remove gallium atoms from the composition.

[†] Trade name.

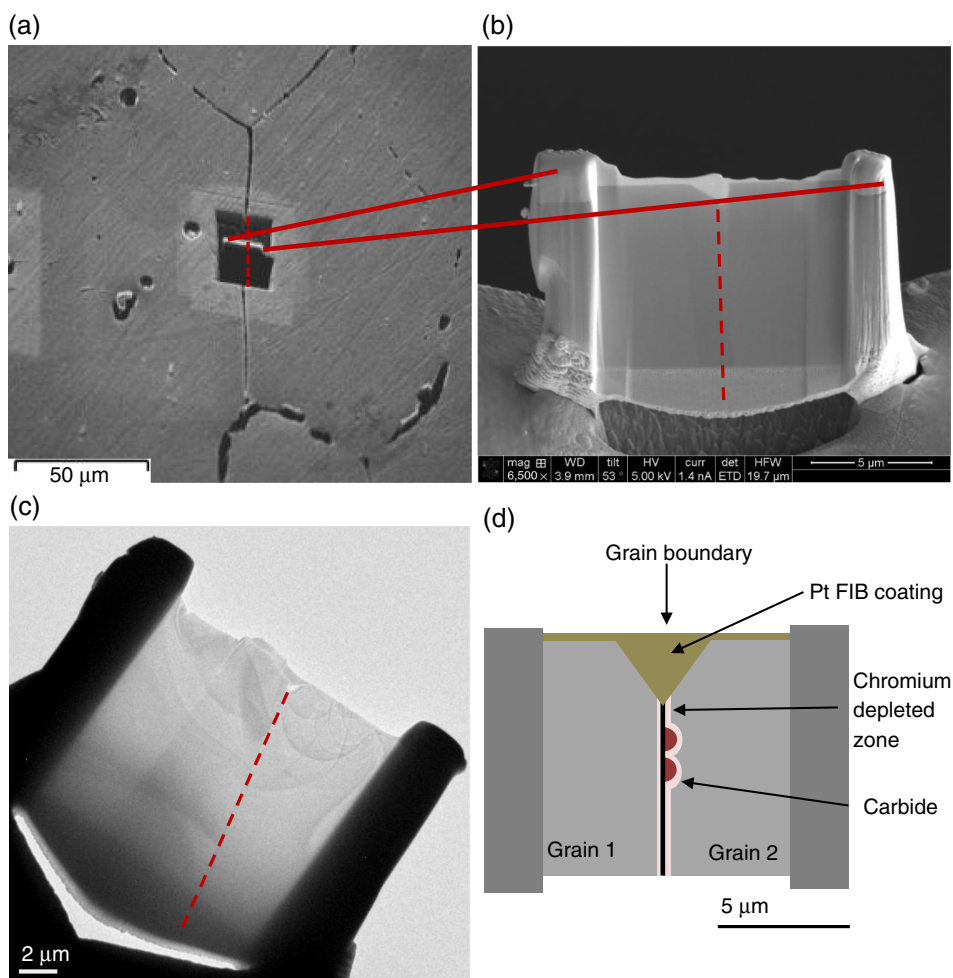


FIGURE 2. (a) SEM image showing a single grain boundary being cut from the bulk sample, (b) the lamellar viewed in SEM comprising the two grains with the grain boundary, indicated by the dotted line down the middle, (c) a sample viewed in TEM again with the dotted line on the grain boundary, and (d) layout of a typical corroded sample.

RESULTS

The annealed and corroded alloy was first examined with EBSD to determine relevant grain boundaries for representative TEM samples. The EBSD OIM produced three maps for each scanned region: the SEM image, OIM image, and the labeled CSL boundaries image, as shown in Figure 3. The same regions mapped in EBSD were later found in the FIB SEM, and known CSL and non-CSL samples were prepared for TEM analysis.

White light interferometry characterized the morphology of corroded boundaries that were both CSL and non-CSL. From the depth and width characterization of corroded crevices, it was determined that CSL boundaries corroded 0.18 μm to 0.96 μm in depth and 1.73 μm to 5.47 μm in width. For non-CSL boundaries, the corrosion depth ranged from 0.38 μm to 3.05 μm and the width ranged from 2.36 μm to 4.91 μm, as summarized in Figure 4. The corrosion depth upper-threshold was observed to be about

1.0 μm in CSL boundaries, whereas non-CSL depth observations showed a much larger and deeper range of crevice depth. The 3D profilometry results indicated that the widths of the corroded grain boundaries were two to five times larger than the corresponding depths.

The initial examination of corroded and immune samples in bright field TEM showed that the corroded boundaries had a wavy structure, later determined to be a result of chromium-rich carbides, whereas immune boundaries were straight without deviations. Representative examples of both are seen in Figure 5. Using EDS maps and line scans in the TEM, the features along the corroded grain boundary were determined to be chromium enhancements, as seen in an example boundary in Figure 6. As shown in Figure 7, the carbide structure was confirmed through diffraction of the two grains and the carbide in between, showing that the intergranular carbides have the expected $M_{23}C_6$ composition. To summarize the standard TEM analysis, all 10 of the corroded boundaries contained chromium-rich carbides dotted along the grain

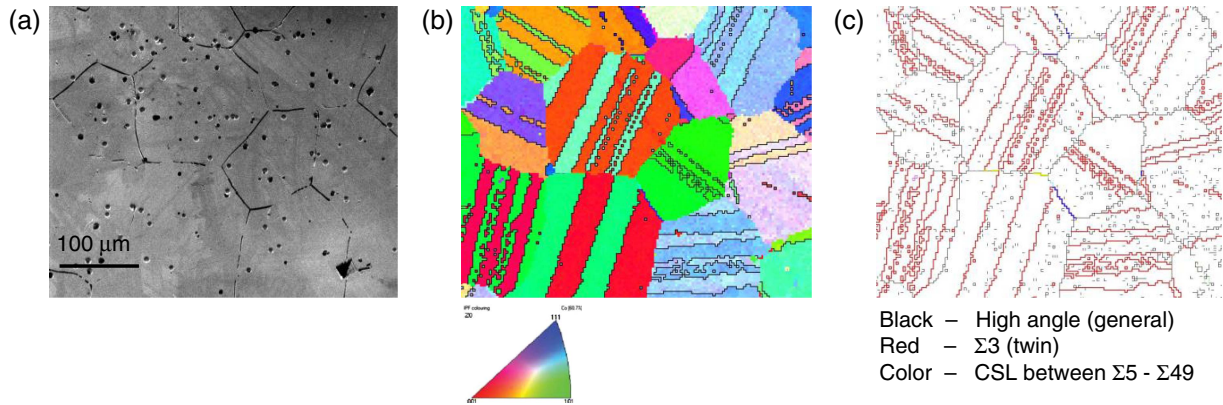


FIGURE 3. The EBSD generated (a) SEM images, (b) OIM images, and (c) labeled CSL boundaries of the scanned region, later identified in the FIB/SEM for TEM sample preparation.

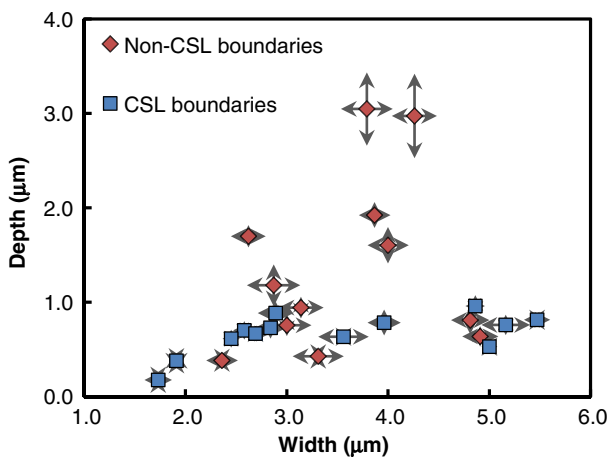


FIGURE 4. Depth and width measurements collected from 3D profilometry showed that the corrosion width was approximately two to five times larger than its corresponding depth. With square as CSL and diamond as non-CSL, each point represents a single boundary, where the arrows represent the range of the multiple measurements along that boundary.

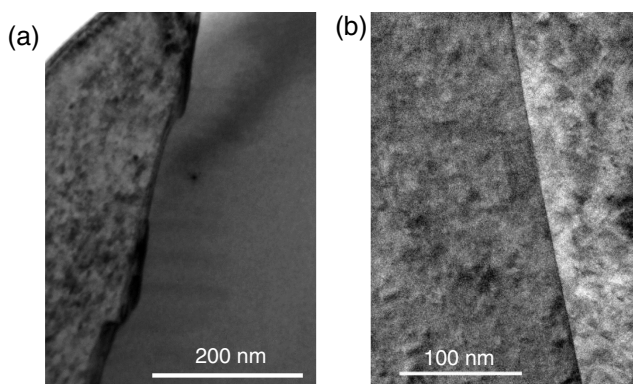


FIGURE 5. The initial examination in bright field TEM showed (a) the corroded boundaries have a wavy structure, where each bend was a carbide feature at the boundary, whereas (b) immune boundaries were straight and featureless.

boundaries, while all five of the CSL immune boundaries did not show carbides, and four of the five immune boundaries did not show carbides. The results of the 22 grain boundary samples are summarized in the chart of Figure 8. The one immune boundary with carbides showed that the carbides were on a size scale around <math><50\text{ nm}</math>, less than half of the size of the other corroded boundaries' carbides.

The chromium-rich carbides were lens shaped and shared epitaxial alignment with the grain on the concave side of the carbides seen in an example boundary in Figures 9 and 10. Figure 9(a) shows a bright field TEM image and Figure 9(b) shows a high-resolution image with the carbide epitaxy to grain 1. Figure 10 shows the same sample, confirming the carbide epitaxy through dark field TEM. In dark field, a particular diffraction spot can be selected and only the grains of that orientation will appear bright. The bump out feature of the carbide was shown when the crystallographic orientation of grain 1 was selected in dark field, in Figure 10(a). When the crystallographic orientation of grain 2 was selected, in Figure 10(b), the carbide feature was dark like the rest of grain 1. This implied that the carbide has the same orientation as grain 1. Comparable carbide shape and evolution has been previously modeled for a copper indium alloy, as diagrammed in Figure 11.⁷² The driving force for carbides to segregate during the initial casting was the reduction of the surface energy between the bulk grains and the grain boundary, replacing a high-energy boundary, α/α' , with a lower one, α/β and α'/β . These carbides formed on the disordered, high-energy boundary, agreeing with other sensitization and CSL models.^{21,67,72}

A representative annular dark field (ADF) and high-resolution EDS map, in Figure 12, shows the lens-shaped chromium-rich carbide at the grain boundary of the CoCrMo alloy. The clearest EDS signal showed the primary elements of the composition, Co, Cr, and Mo, as maps and with a quantized chart from key regions in

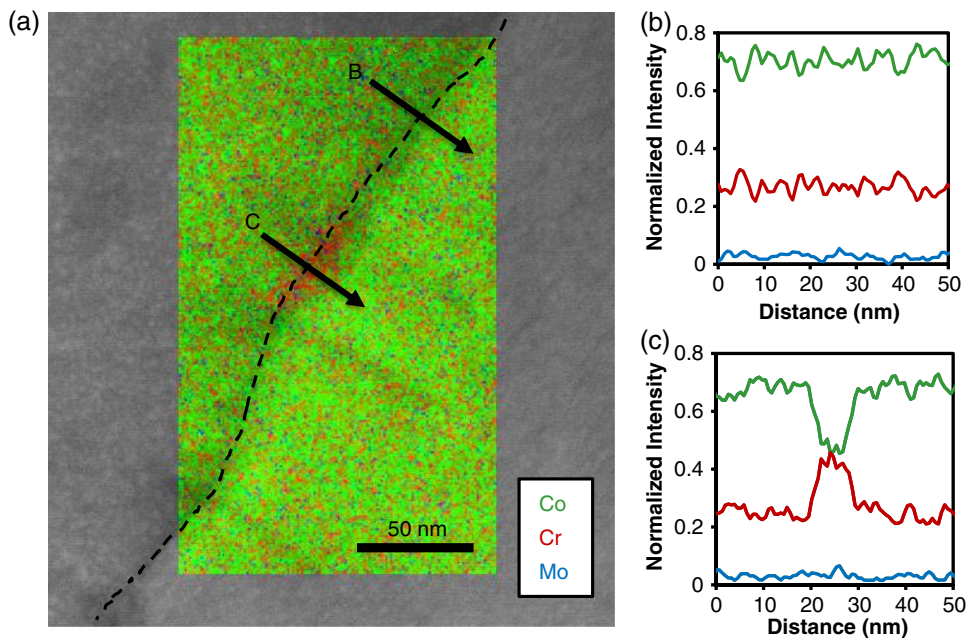


FIGURE 6. (a) Bright field TEM image with an EDS map, Co = green, Cr = red, and Mo = blue. The dotted line indicates the grain boundary, with a chromium enhancement. Line scans (b) and (c) indicate the change in concentration at the carbide.

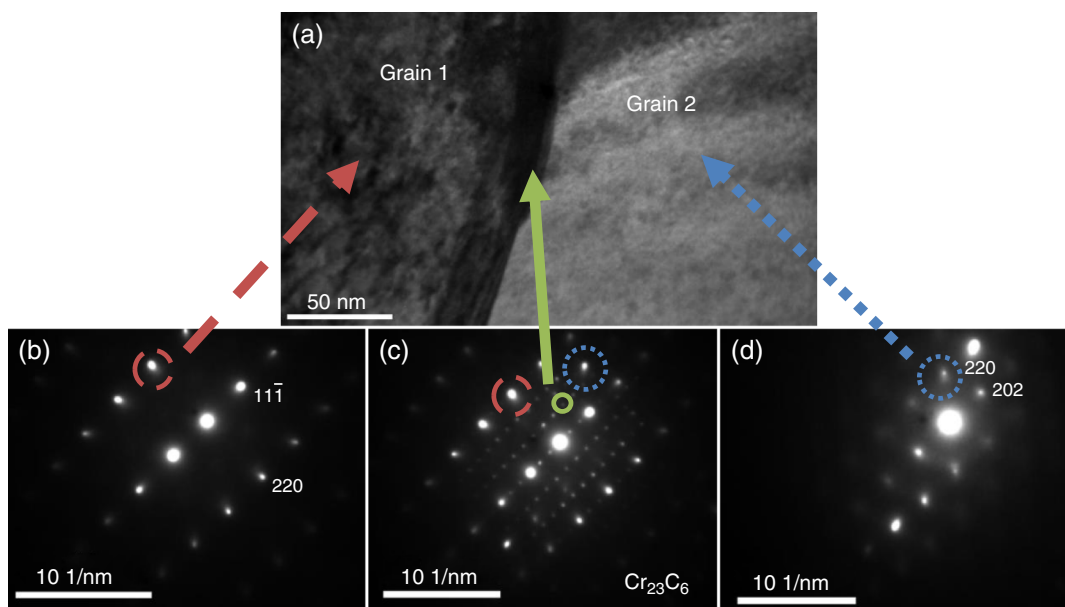


FIGURE 7. (a) Bright field image of a grain boundary showing the chromium-rich carbide feature. (b) Diffraction pattern of grain 1, (c) diffraction pattern of the feature showing a $M_{23}C_6$ carbide grain structure, and (d) diffraction pattern of grain 2.

Table 2. The area around the carbide was a CDZ, i.e., the chromium composition was reduced around the carbide and along the grain boundary. The depleted zone normal to the grain boundary plane was at the same length scale as the width of the carbides, about ~10 nm, seen in the line scan in Figure 12(b). For another carbide map in Figure 13, the CDZ extended along the grain boundary with a comparable length scale to the length of the carbide, with compositions at

these regions quantized in Table 3. This is seen in the maps, but was confirmed through the quantified EDS regions. For the four samples examined in high-resolution EDS, scans were taken along two to five carbides of each sample, with the average carbide composition, matrix composition, and depleted zone compositions shown in Table 4. For the singular immune sample with carbides, the <50 nm carbides were included in the EDS scans. For these carbides,

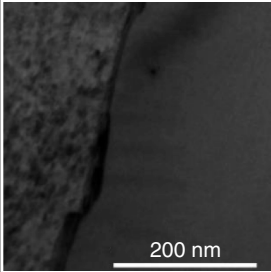
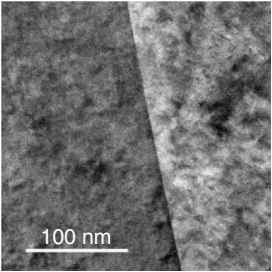
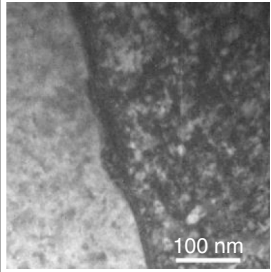
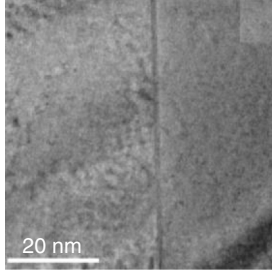
	Corroded	Immune
Non-CSL boundary	Carbides (N = 10) No carbides (N = 0) 	Carbides (N = 1) No carbides (N = 4) 
CSL boundary	Carbides (N = 2) No carbides (N = 0) 	Carbides (N = 0) No carbides (N = 5) 

FIGURE 8. The chart summarizes the samples measured in each category and if carbides were present. The boundary can be either CSL or non-CSL, and either be corroded or immune. The proportion of samples in each category represents the approximate frequency seen in the bulk sample.

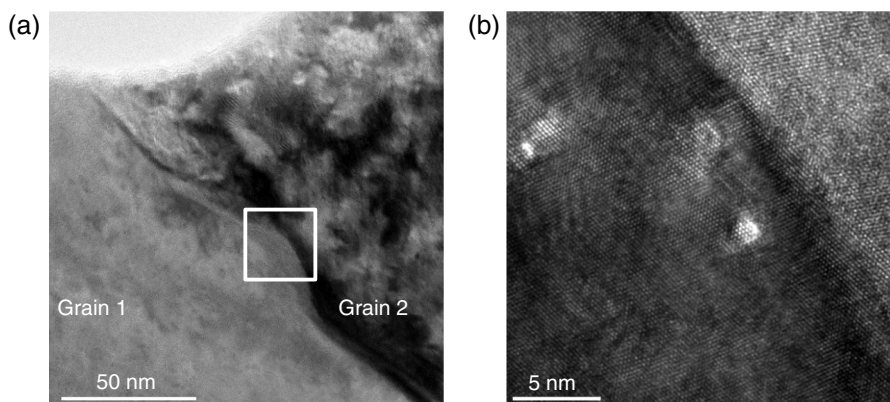


FIGURE 9. (a) The lens shape of the chromium-rich carbide with (b) the high-resolution transmission electron microscope showing the shared epitaxial alignment with the concave grain.

the chromium depletion, i.e., the difference in the matrix chromium composition and the chromium composition along the grain boundary, was less than 2 at%, shown in Figure 14 and composition in Table 5. This size of carbide hit a threshold to no longer cause a true CDZ, which left that grain boundary without a CDZ and therefore immune.

Note that the size/volume fraction of the carbides scales approximately corresponded with the chromium depletion near them; larger carbides caused

larger chromium depletion. This indicates that there was a local “chromium conservation” in regions 20 nm to 40 nm on either side of the grain boundaries and no long-range diffusion of chromium, at least for the conditions used to make the samples.

APT complemented the EDS results; a region containing a grain boundary and a carbide is shown in Figure 15. The shape of the carbide was ~60 nm along the boundary by ~10 nm wide, with a similar lens shape to those observed via electron microscopy. A line scan

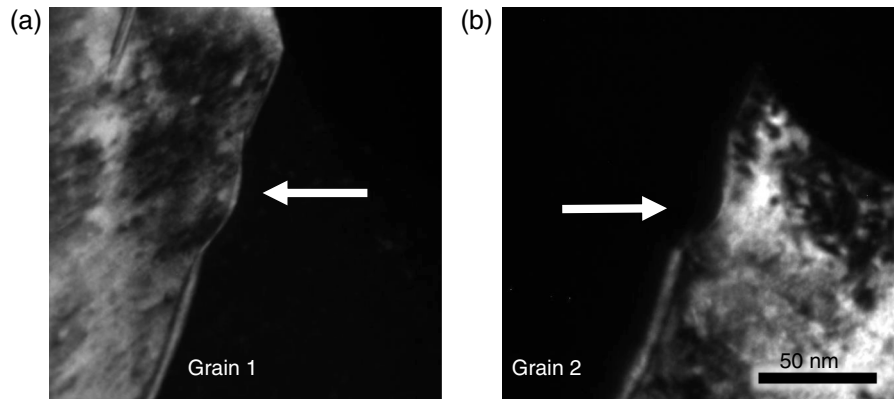


FIGURE 10. Dark field selecting for (a) grain 1 and (b) grain 2, showing the epitaxial nature of the chromium-rich carbide to the grain on the concave side of the lens.

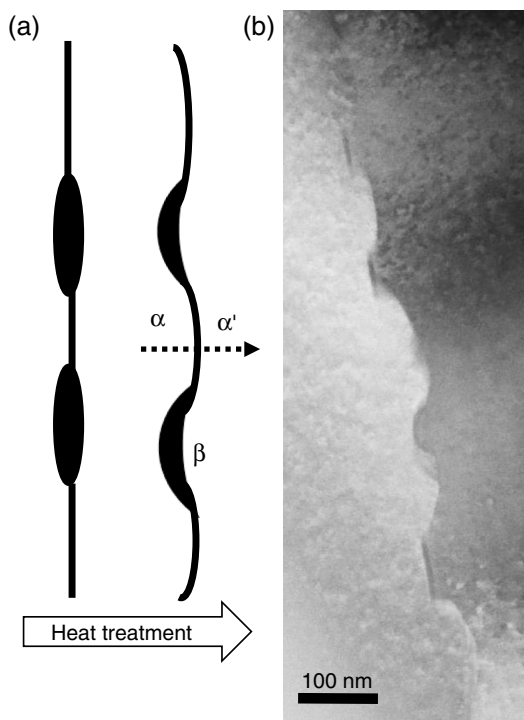


FIGURE 11. The distinct shape of the chromium-rich carbides has been previously modeled by a copper indium alloy, with α as the trailing grain, α' as the forward grain, and β as the carbide.⁷²

taken through the slice, as shown in Figure 15(b), shows that the composition of the matrix was 30 at% Cr and the composition in the carbide was 90 at% Cr; the exact composition with a high accuracy could not be determined because of uneven evaporation from the sample.

GRAIN BOUNDARY ASSISTED CREVICE CORROSION MODEL

Having now presented the experimental results, the focus turns to developing a general model for

corrosion associated with nanoscale precipitates to connect nanoscale segregation to corrosion. As mentioned earlier, the primary focus of the current literature has been on large precipitates at grain boundaries, two to three orders of magnitude larger than what was observed. These micrometer carbides lead to extensive regions of chromium depletion, and the detailed mechanism of sensitization is not necessarily the same for the samples herein; less segregation was found that was also spatially inhomogeneous. Prior models need to be extended to finer-scale segregation. This paper will first consider just the grain boundary component, showing that both the grain boundary energy and local chromium concentration play a role in corrosion properties. Then, the model will be extended to include local crevice corrosion for a more complete description.

Local Grain Boundary Attack

The first step is to model how the nanoscale segregation and grain boundary energy impact corrosion initiation; an understanding is needed as to whether the energy change for corrosion resulting from local chromium depletion dominates the energy resulting from removal of the grain boundary. Figure 16 shows the differences between macro and nano versions of corrosion. For macro-sensitization, the composition is so chromium depleted that the protective oxide does not form. This model does not scale to the nanoscale as the depletion was on too small of a size scale to significantly change the oxide coverage. Chromium oxide growth over nanoscale depleted regions have been shown for regions <20 nm in CrZr alloys⁷³ and for other alloys,⁷⁴ so this is a reasonable assumption of oxide overgrowth in the CDZ of ~10 nm. Instead of a broken CrO_2 oxide layer, the focus is on the grain boundary energy and chromium depletion magnitude at the boundary by comparing the grain boundary energy for CSL and non-CSL with the grain boundary energy effect of a CDZ.

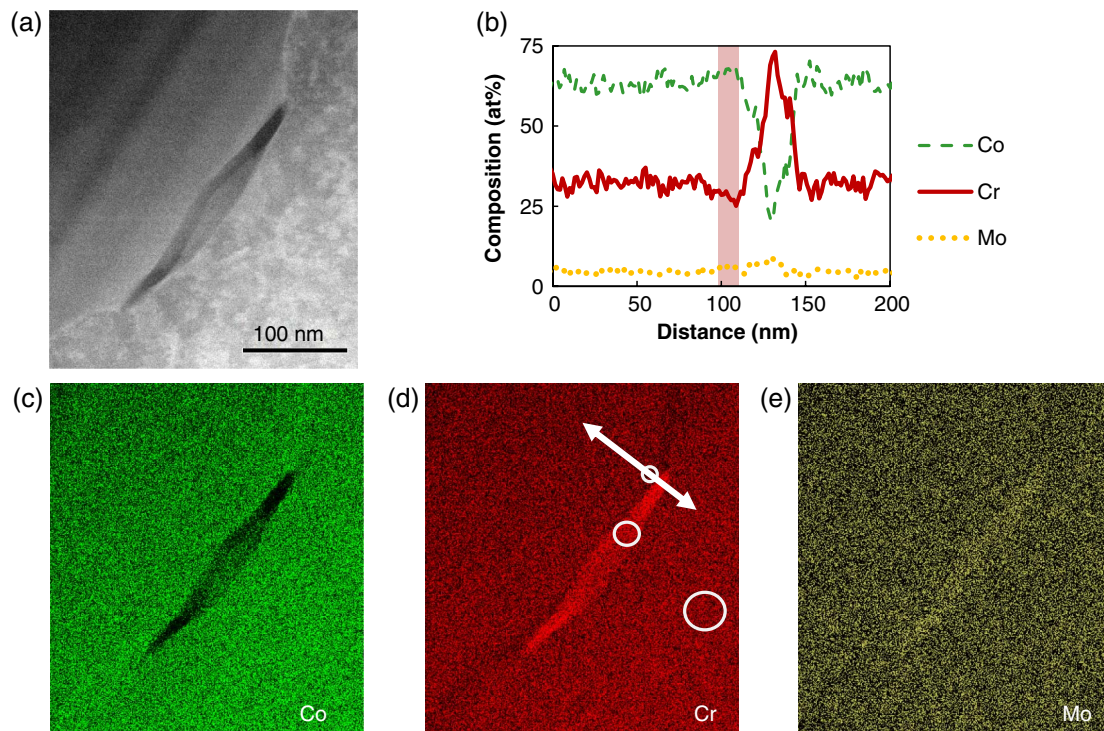


FIGURE 12. The chromium depleted region around a chromium-rich carbide, with (a) the ADF image, (b) an extracted line scan to show the CDZ, (c) cobalt, (d) chromium, and (e) molybdenum. The arrow indicates where the line scan was taken, and the circles indicate where the EDS spectra were quantized, reported in Table 2.

TABLE 2
EDS Quantification, Figure 12 Carbide

	Co (at%)	Cr (at%)	Mo (at%)
Matrix	62.5	33.6	2.9
Carbide	18.7	73.8	8.0
CDZ	68.3	23.0	5.1

To be specific, the difference in composition between the chromium depleted and matrix compositions leads to a difference in the corrosion potentials that

affected the dissolution of the CoCrMo alloy. The main composition change was a CDZ next to a chromium-rich $M_{23}C_6$ carbide. There is an enhancement of Mo in the $M_{23}C_6$ carbide, a common result of alloys with both Mo and Cr in the $M_{23}C_6$ carbides, but no difference in the CDZ. The Mo concentration does not change in the CDZ, so the average composition of the matrix and CDZ is renormalized to be just Co and Cr.

It has been previously shown that as the chromium content of an alloy decreases the corrosion potential increases,⁷⁵⁻⁷⁶ and here it can be

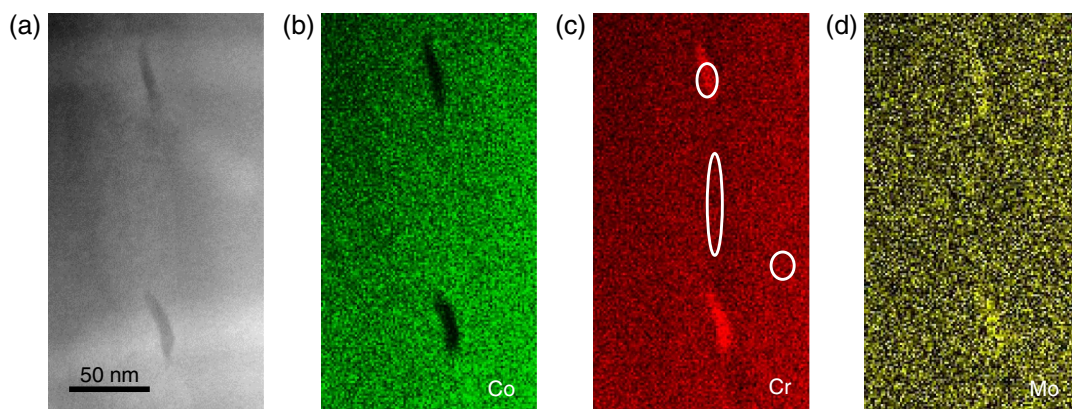


FIGURE 13. The chromium depleted region between two chromium-rich carbides, with (a) the ADF image, (b) cobalt, (c) chromium, and (d) molybdenum. The chromium depletion is measured along a 150 nm section of grain boundary between two carbides and found to be sensitized by 2%. The circles indicate where the EDS spectra were quantized in Table 3.

TABLE 3
EDS Quantification, Figure 13 Carbide

	Co (at%)	Cr (at%)	Mo (at%)
Matrix	62.5	31.1	4.2
Carbide	37.5	53.7	6.7
CDZ	64.3	29.1	4.2

TABLE 4
Summary of Averaged EDS Quantifications

	Co (at%)	Cr (at%)	Mo (at%)
Matrix	62.9±1.5	30.6±1.4	4.4±0.7
Carbide	29.6±7.8	62.4±8.9	7.8±1.2
CDZ	69.2±2.7	23.8±2.19	4.2±0.9

approximated that the CoCrMo alloy would follow a similar trend. In Kelly, et al.,⁷⁵ an Fe-Cr alloy with 20 at% Cr corrodes at -370 mV_{SCE} and the alloy with 14 at% Cr corrodes at -310 mV_{SCE}. At this level of chromium depletion, the corrosion potential increases 10 mV per 1 at% Cr decrease. Using the EDS data of the quantified chromium depletion zone, the chromium reduction on average was 7.1 at% Cr. The change in corrosion potential from the matrix to the CDZ would be 71 mV, designated as $\Delta\mu$.

$$\Delta\mu = \mu_{\text{matrix}} - \mu_{\text{CDZ}} \quad (1)$$

$$\Delta\mu = -71 \text{ mV} \quad (2)$$

The electrochemical difference was converted to joules using a weighted average for composition for the charge unit of Co and Cr.

$$\Delta\mu = -71 \text{ mV} \times 2.3e = -0.1633 \text{ eV} \quad (3)$$

$$\Delta\mu = 2.61 \times 10^{-20} \text{ J} \quad (4)$$

With the electrochemical potential difference of the matrix and the CDZ, the difference in grain boundary energy between these two compositions was calculated. The parameters considered for the model are shown in Figure 17, with L the width of the

CDZ, a the distance between atoms along the grain boundary, b the distance between atoms perpendicular to the grain boundary, and d the depth of corrosion set to one monolayer. The energy of the grain boundary ΔE_{GB} and energy lost as a result of the chromium depleted zone ΔE_{CDZ} per unit length of both were defined as:

$$\Delta E_{\text{GB}} = -\gamma_{\text{GB}}d \quad (5)$$

$$\Delta E_{\text{CDZ}} = \Delta\mu \frac{L}{ab} \quad (6)$$

The interfacial grain boundary energy was approximated using the molecular dynamics results of a Fe-Cr system with 30 at% Cr, as Fe and Co have the same surface energy values as pure materials.⁷⁷⁻⁷⁸ The weighted average of the atomic diameters of Co and Cr is 0.382 nm, and this value was used for a, b, and d. The γ_{GB} of the CoCrMo grain boundaries varies from 0.4 J/m^2 to 1.4 J/m^2 . The average chromium depletion change was found to be 7.1 at%, and less extreme areas were found with Cr reduction as low as 3 at% ($\Delta\mu = -30$ mV), so this range can be used as a conservative estimation. The width of the CDZ ranged from 5 nm to 10 nm. Therefore, the grain boundary energy and the depletion energy reduction ranges were calculated as:

$$\Delta E_{\text{GB}} = -1.53 \times 10^{-7} \frac{\text{mJ}}{\text{m}} \text{ to } -5.35 \times 10^{-7} \frac{\text{mJ}}{\text{m}} \quad (7)$$

$$\Delta E_{\text{CDZ}} = -3.78 \times 10^{-7} \frac{\text{mJ}}{\text{m}} \text{ to } -17.9 \times 10^{-7} \frac{\text{mJ}}{\text{m}} \quad (8)$$

As these ranges overlap, the model indicates that both the intrinsic grain boundary energy as well as the local chromium depletion are relevant, unlike the

TABLE 5
EDS Quantification, Figure 14 Carbide

	Co (at%)	Cr (at%)	Mo (at%)
Matrix	64.5	31.5	3.9
Carbide	56.5	39.0	4.5
CDZ	67.0	30.0	3.3

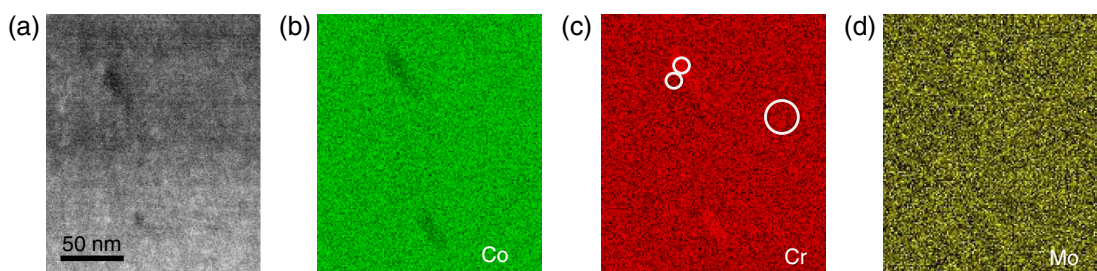


FIGURE 14. Carbides less than ~ 50 nm did not show measurable chromium depletion, with (a) the ADF image, (b) cobalt, (c) chromium, and (d) molybdenum. The circles indicate where the EDS spectra were quantized in Table 5.

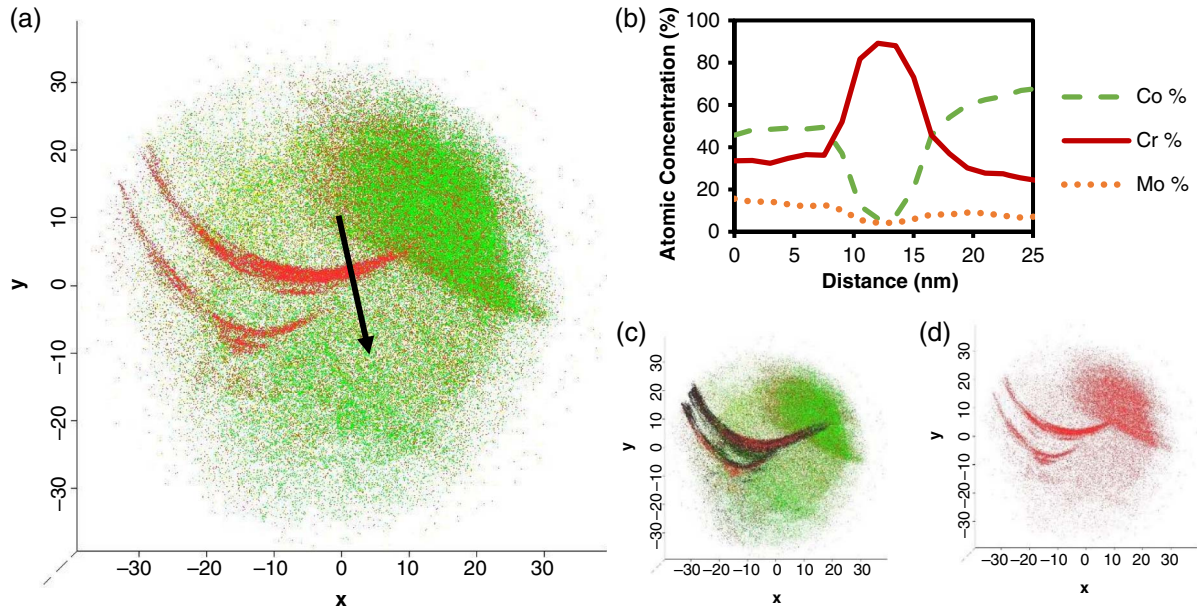


FIGURE 15. (a) A 10-nm thick slice of LEAP acquisition that intersected with a grain boundary and a carbide. (b) Composition profile through the edge of the carbide showing the chromium segregation. (c) The gallium present from FIB thinning segregated to the boundaries in the sample (black), which leaves a track of where the grain boundary is located. (d) The chromium concentration evaporating mainly at the grain boundaries of the carbide with a patch of uneven evaporation on the edge.

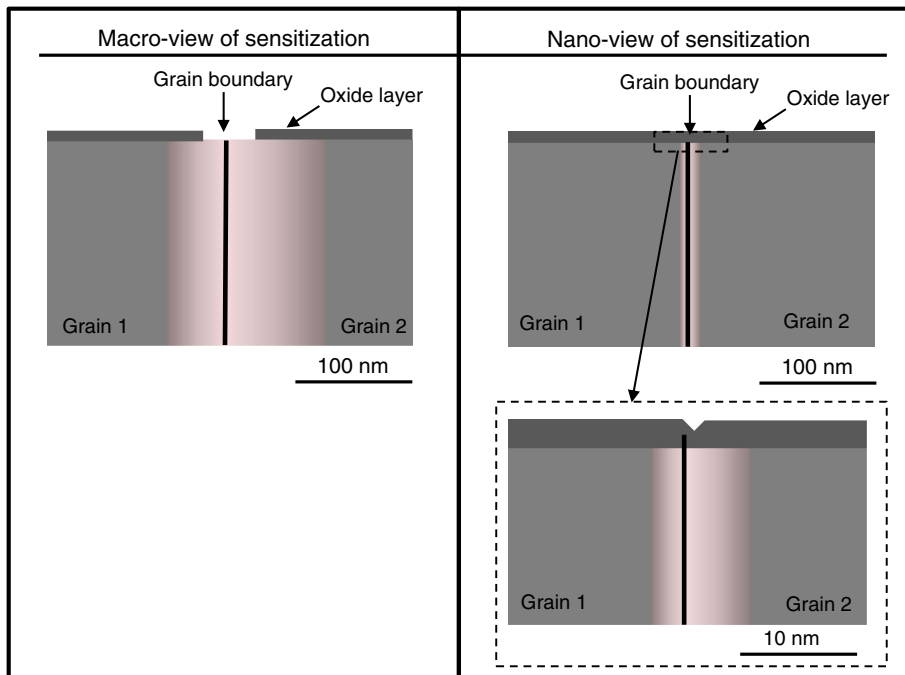


FIGURE 16. The macro-view of sensitization has large regions of chromium depletion, leading to incomplete oxide formation around the sensitized boundary. In nanoscale sensitization, the oxide is not significantly diminished. The chromium depletion is on a nanometer scale along the boundary.

case for very large precipitates as mentioned earlier. High-energy boundaries without chromium depletion would show preferential attack, as would low-angle boundaries with some level of depletion. However, as

indicated in the experimental results section, the precipitates occur more at the high-energy boundaries. It is concluded that for the nanoscale precipitates herein both factors influenced corrosion sensitivity.

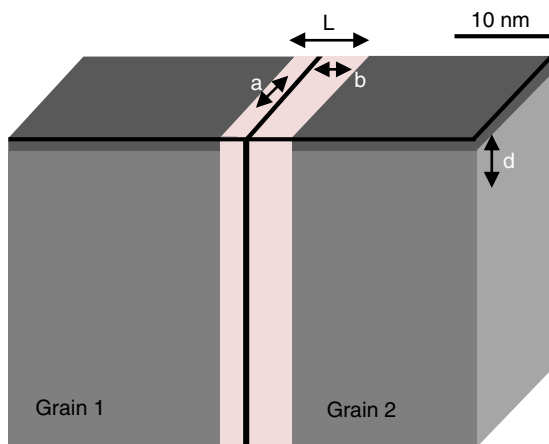


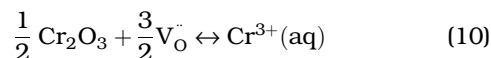
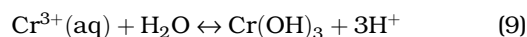
FIGURE 17. The model for grain boundary assisted crevice corrosion includes the CDZ width (L), the distance between atoms along the grain boundary (a), the distance between atoms perpendicular to the grain boundary (b), and the depth of one monolayer of atoms removed from the surface (d). The weighted average diameter of Co and Cr can be used for a , b , and d , while L is measured from the EDS maps.

Including the Role of Crevice Corrosion

The compositional depletion and the energy gain from removing the boundary provides the driving force for the initial attack at the grain boundary, but this does not fully explain the experimental data. The dissolution rates for crevices and pits have long been linked to kinetic Wulff models that show the shape of a crevice is dependent on individual dissolution rates along various directions.⁷⁹ In the present alloy, both the dissolution rate down the boundary, which affects the depth, and the dissolution rate normal to the boundary, which will influence the width, are used. If the local energy terms were the only driving force, the attack

would be straight down the boundary and approximately as wide as the width of the CDZ. This, however, was not the case; the width of the attack was orders of magnitude larger than the depletion zone. Hence, once attack has initiated at the boundary, a second mechanism has to be dominant.

The model needs to be expanded to include the crevice corrosion that develops around the grain boundaries. In crevice corrosion, the degrading environment is a confined volume. As the corrosion begins, the pH drops and hydrogen ions are created (Equation [9]), which accelerates corrosion. In addition to the chromium ions, albumin protein, sodium, potassium, and chlorine were also present during electrochemical testing. Diffusion in the crevice can limit the reactions occurring, as illustrated in Figure 18. To proceed in crevice corrosion, chromium ions must come from the surface, yet if this reaction is quenched, a back reaction producing chromium oxide and oxygen vacancies will cause the corrosion to stop (Equation [10]).



Evidence can be seen for this crevice corrosion in the results of the crevice width-depth data shown in Figure 4. Overall, the widths of the corroded boundaries were two to five times larger than the depths. This is reasonable because the boundaries were undergoing only mild chemical segregation, compared to typically studied levels of sensitization for much larger precipitates in the literature. Other crevice trends observed can be further understood. As seen in the TEM images, the carbides were inhomogeneously spaced along the

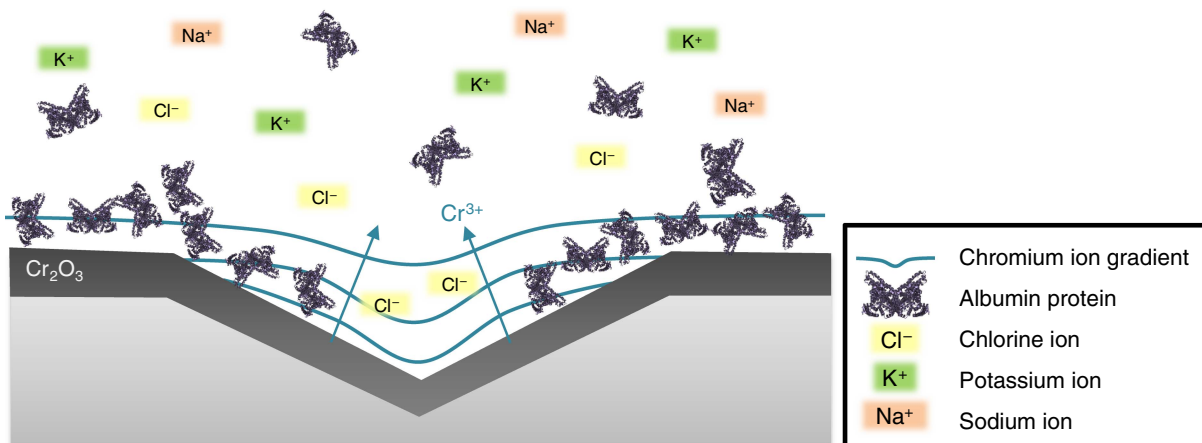


FIGURE 18. The chromium oxide layer with the light gray representing the bulk, the dark gray representing the oxide, the black arrows representing the Cr^{3+} movement, and the blue lines representing the CrOH^{2+} concentration. As the chromium dissolution products accumulate in the crevice, the reaction down is quenched and the corrosion occurs out toward the walls of the crevice. The ions and albumin proteins are not to scale, but to serve as a representation. In the human body, many more ions and proteins would be present.

boundaries. With local grain boundary nucleation followed by crevice corrosion, the model predicts that, depending on the local carbide concentration, there would be fluctuations in both the depth and width corrosion driving forces. As confirmed in the data, for all boundaries there were large local fluctuations in the width and depth, represented by the arrows' ranges of each data point in Figure 4. Differences in carbide concentrations were also observed for corroded CSLs and non-CSLs, with corroded CSLs containing smaller and fewer carbides. The model predicts that non-CSLs would have lower width to depth ratios, and indeed that is seen in the width-depth data. This was also seen in the depth data, as most CSLs only corrode to about 1 μm , with widths from 2 μm to 5 μm . Non-CSLs, on the other hand, corroded down to 3 μm , with widths from 3 μm to 5 μm . The carbides provided a larger driving force down the boundary in these non-CSL cases, consistent with the model.

By combining grain boundary sensitization and the crevice corrosion into the GACC model, it is possible to link the depth and width driving forces for corrosion to understand the behavior observed in the CoCrMo alloy grain boundaries with the nanoscale precipitates.

DISCUSSION

It has been demonstrated herein that chromium depletion in these CoCrMo alloys occurs at the nanoscale. The nanoscale chromium-rich carbides combine with the grain boundary properties to affect the localized corrosion susceptibility. The precipitates by themselves are not the full story, unlike in the case with conventional and more macroscopic precipitation studies present in the literature. With the GACC model, it is interpreted that the CDZ led to the start of a crevice at the grain boundary, which then led to runaway corrosion at that location. The GACC model accounts for why some higher level CSLs were seen to corrode: if they had a carbide sensitizing one region of the exposed boundary, it was enough to initiate corrosion. This paper has only reported on high-angle semi-random grain boundaries; in a future publication, additional details on lower energy grain boundaries will be described.

Other models have recognized the difference between the CDZ and the actual corroded crevice.^{30,63} For this paper's CoCrMo alloys, the depletion of chromium was ~1 nm to 10 nm in width, while the crevice on top of the trench was as wide as 5 μm . While previous models did not link these two results, the width-depth ratio data were linked to the width dissolution rate and the basic diffusion in the crevice. Using the width-depth measurements across many crevices, it was concluded that the width corrosion was a result of the quenched depth corrosion, causing both driving forces to occur, but with stronger width

corrosion. This width-depth ratio data provided cross-verification of the GACC model.

To compare with the existing literature, established minimum chromium composition levels are sought. For CoCr bimetallics, the minimum Cr to prevent corrosion is not well established, reported at 20% or 30% Cr.⁸⁰⁻⁸¹ Stainless steel was reviewed for a more thoroughly studied material for comparison. In stainless steel models, it was known that stainless steel has a composition around 19 at% Cr and a sensitization with CDZs around 13 at% Cr.^{30,48,63-65} This drop is a 6 at% composition drop or a 32% reduction in chromium. This can be compared to the EDS data of the matrix and CDZ of the samples. The matrix compositions across the CoCrMo alloy samples matched the expected values for the composition, with a standard deviation of 1.3 at%, approximately equal to the 1% expected error with EDS. The largest standard deviation came from the carbide cobalt and chromium values, which was not surprising as the thickness of the carbides and the thickness of the sample above and below the carbide varied. Therefore, the EDS spectra measured an uncontrolled ratio of the carbide and the matrix, causing a large variance of the carbide compositions. The CDZ mapping showed an average composition of 23.8 at% Cr, a 6.8 at% composition drop of a 22% decrease in chromium from the matrix composition of 30.6 at% Cr. The results for chromium depletion measurements suggested that a smaller change than the 32% reduction proposed for stainless steels has an effect on the corrosion performance in CoCrMo alloys.

While these comparisons are useful, it needs to be noted that to come close to physiological conditions the corrosion tests were performed in a BCS with a protein content of 30 g/L, buffered to a basic pH of 7.4 solution with phosphate-buffered saline. This is an accepted approximation for the conditions in vivo, and it is well established that one cannot simply use, for instance, salt solutions and obtain physiologically relevant results. The BCS solution contains albumin proteins, sodium, potassium, and chlorine ions as well as lipids, vitamins, amino acids, attachment factors, growth factors, hormones, and other components essential for cell growth. It is certainly far from a simple electrolytic solution, so there may well be substantial differences in the detailed electrochemical processes taking place. The solution may also be evolving in time, as previous studies have shown the roles of proteins and molybdates in the electrochemical properties of CoCrMo alloys and their metal oxide behavior;⁸² within those experiments indications that molybdates released from the metal were leading to cross-linking of the proteins.

The idea of comparing orientational grain boundary energy and electrochemical energy differences based on the differences in corrosion potential of the compositions is an initial model that needs

expansion. Much more is occurring at the surface and at the grain boundaries as CoCrMo corrodes in the human body. To list only a few, there may be contributions from surface energy changes resulting from protein adsorption, catalytic decomposition (denaturing) of proteins, and the formation of protective graphitic layers.⁸³ For hip implants, both mechanical wear and corrosion need to be considered for performance.⁸⁴ In this work, the electrochemical corrosion test is a static test without tribological wear occurring; Mathew, et al., has shown the synergistic corrosion effects of the physiological solution and triboactivity.⁸⁵⁻⁸⁶ There may also be important issues related to fretting assisted corrosion particularly at the junctions of modular devices. These will be left to future work.

It is useful to make a few comments about what compositions should be used for implant materials. The results of this work indicate that more precise specifications are needed for the CoCrMo alloys used for implants. In the 1970s, sensitized stainless steels were used as poorly performing implant material before more routine structural sampling was used to ensure that intergranular corrosion would not be immediately detrimental to implant integrity.¹⁹ Great advancements, especially in stainless steels, have allowed for ways to control carbides and CDZs through temperature and length of processing times, yet this understanding needs to be extended to nanoscale carbides and to CoCrMo alloys. The ASTM standard that dictates the CoCrMo for surgical implants specifies that the material must "have a homogeneous microstructure with an average grain size of ASTM No. 5 or finer."⁶⁸ This standard neglects the presence of precipitated carbides, and the acceptable size and regions of a CDZ. The nanostructure must be analyzed as well. Nanoscale analysis must be used for characterization, as the CDZs measured in this work were shown to have significant effects on the corrosion properties. The CoCrMo alloy nanostructure would therefore affect the in vivo performance properties.

For future hip implants, perhaps precisely engineered CoCrMo alloys with suitable heat treatments could be designed, as the metallurgical structure could be controlled at the microscale down to the nanoscale, including the potential to control corrosion through grain boundary engineering.^{55,58-60} Controlling the CSLs could lead to a metal designed with controlled surface grains. The material on the surface could be protective by controlling the carbide presence and the CDZs that would lead to a well-performing alloy, even if the material has internally sensitized regions.

CONCLUSIONS

❖ Chromium depletion occurs in this CoCrMo alloy, and it can occur on the nanoscale. The nanoscale chromium-rich carbides and the grain boundary

geometry both determine the localized corrosion susceptibility.

❖ The grain boundary assisted crevice corrosion (GACC) model explains how the chromium depleted zones initiate corrosion at particular grain boundaries, which is then further propagated by crevice corrosion.

ACKNOWLEDGMENTS

We thank Pooja Panigrahi for the samples used in this study, and thank ATI Allvac for the original donation of the alloy materials. EEH is supported by the Department of Defense (DoD) through the National Defense Science and Engineering Graduate Fellowship (NDSEG) program. This research was funded by the National Science Foundation on grant number CMMI-1030703.

REFERENCES

1. S. Kurtz, K. Ong, E. Lau, F. Mowat, M. Halpern, *J. Bone Joint Surg.* 89, 4 (2007): p. 780-785.
2. B. Bashinskaya, R.M. Zimmerman, B.P. Walcott, V. Antoci, *ISRN Orthop.* 2012 (2012): p. 185938.
3. S. Pramanik, A.K. Agarwal, K.N. Rai, *Trends Biomat. Artif. Organs* 19, 1 (2005): p. 15-26.
4. A.J. Clemow, B.L. Daniell, *J. Biomed. Mater. Res.* 13, 2 (1979): p. 265-279.
5. M. Gomez, H. Mancha, A. Salinas, J. Rodrigues, J. Escobedo, M.R. Castro, M. Mendez, *J. Biomed. Mater. Res.* 34, 2 (1997): p. 157-163.
6. J. Nevelos, J. Shelton, J. Fisher, *Hip Int.* 14 (2004): p. 1-10.
7. B.D. Ratner, A.S. Hoffman, F.J. Schoen, J.E. Lemons, *Biomaterials Science: An Introduction to Materials in Medicine*, 2nd ed. (London, United Kingdom: Academic Press, 2004).
8. A.J. Saldivar-Garcia, H.F. Lopez, *J. Biomed. Mater. Res. A* 74, 2 (2005): p. 269-274.
9. W.M. Mihalko, M.A. Wimmer, C.A. Pacione, M.P. Laurent, R.F. Murphy, C. Rider, *Clin. Orthop. Relat. Res.* 472, 12 (2014): p. 3747-3758.
10. N. Hallab, K. Merritt, J.J. Jacobs, *J. Bone Joint Surg. Am.* 83, 3 (2001): p. 428-436.
11. J.L. Gilbert, C.A. Buckley, J.J. Jacobs, *J. Biomed. Mater. Res.* 27, 12 (1993): p. 1533-1544.
12. Y. Yan, A. Neville, D. Dowson, S. Williams, *Tribol. Int.* 39, 12 (2006): p. 1509-1517.
13. J. Gilbert, S. Mali, R.M. Urban, C. Silverton, J.J. Jacobs, *J. Biomed. Mater. Res. B* 100, 2 (2012): p. 584-594.
14. K. Merritt, S.A. Brown, *Clin. Orthop. Relat. Res.* 329 (1996): p. S233-S243.
15. W.C. Witzleb, J. Zeigler, F. Krummenauer, V. Neumeister, K.P. Guenther, *Acta Orthop.* 77, 5 (2006): p. 697-705.
16. P.A. Vendittoli, S. Mottard, A.G. Roy, C. Dupont, M. Lavigne, *J. Bone Joint Surg. Br.* 89, 4 (2007): p. 441-448.
17. H.C. Amstutz, P.A. Campbell, F.J. Dorey, A.J. Johnson, A.K. Skipor, J.J. Jacobs, *J. Arthroplasty* 28, 4 (2013): p. 695-700.
18. E. Bain, R. Aborn, J. Rutherford, *Trans. Am. Soc. Steel Treating* 21, 1 (1933): p. 481-509.
19. E. Smethurst, R.B. Waterhouse, *J. Mater. Sci.* 12, 9 (1977): p. 1781-1792.
20. H.E. Placko, S.A. Brown, J.H. Payer, *J. Biomed. Mater. Res.* 39, 2 (1998): p. 292-299.
21. G. Palumbo, K.T. Aust, *Acta Metall. Mater.* 38, 11 (1990): p. 2343-2352.
22. S.M. Bruemmer, L.A. Charlot, *Scrip. Metall. Mater.* 20, 7 (1986): p. 1019-1024.
23. J.J. Jacobs, R.M. Urban, J.L. Gilbert, A.K. Skipor, J. Black, M. Jasty, J.O. Galante, *Clin. Orthop. Relat. Res.* 319 (1995): p. 94-105.
24. J.J. Jacobs, J.L. Gilbert, R.M. Urban, *J. Bone Joint Surg.* 80, 2 (1998): p. 268-282.
25. L.C. Julian, A.I. Munoz, *Tribol. Int.* 44, 3 (2011): p. 318-329.

26. C.V. Vidal, A.I. Munoz, *Electrochim. Acta* 54, 6 (2009): p. 1798-1809.
27. M. Hernandez-Rodriguez, R. Mercado-Solis, A. Perez-Unzueta, D. Martinez-Delgado, M. Cantú-Sifuentes, *Wear* 259, 7 (2005): p. 958-963.
28. E.L. Hall, C.L. Briant, *Metall. Trans. A* 15, 5 (1984): p. 793-811.
29. C.L. Briant, P.L. Andresen, *Metall. Trans. A* 19, 3 (1988): p. 495-504.
30. C. Stawstrom, M. Hillert, *J. Iron Steel Inst.* 207 (1969): p. 77-85.
31. V.Y. Gertsman, S.M. Bruemmer, *Acta Mater.* 49, 9 (2001): p. 1589-1598.
32. C.L. Briant, *Metall. Trans. A* 18, 4 (1987): p. 691-699.
33. G. Song, A. Atrens, *Adv. Eng. Mater.* 9, 3 (2007): p. 177-183.
34. G.L. Song, A. Atrens, *Adv. Eng. Mater.* 5, 12 (2003): p. 837-858.
35. N. Winzer, A. Atrens, G.L. Song, E. Ghali, W. Dietzel, K.U. Kainer, N. Hort, C. Blawert, *Adv. Eng. Mater.* 7, 8 (2005): p. 659-693.
36. M.C. Zhao, M. Liu, G.L. Song, A. Atrens, *Corros. Sci.* 50, 7 (2008): p. 1939-1953.
37. R. Houdremont, H. Bennek, *Stahl Eisen* 52 (1932): p. 660.
38. V. Kain, R.C. Prasad, P.K. De, *Corrosion* 58, 1 (2002): p. 15-37.
39. W. Clarke, R. Cowan, W. Walker, *Intergranular Corrosion of Stainless Alloys*, ASTM STP 656 (West Conshohocken, PA: ASTM International, 1978), p. 99.
40. R. Singh, S.G. Chowdhury, B.R. Kumar, S.K. Das, P.K. De, I. Chatteraj, *Scrip. Mater.* 57, 3 (2007): p. 185-188.
41. R. Singh, B. Ravikumar, A. Kumar, P.K. Dey, I. Chatteraj, *Metall. Mater. Trans. A* 34, 11 (2003): p. 2441-2447.
42. Y. Zhou, K.T. Aust, U. Erb, G. Palumbo, *Scrip. Mater.* 45, 1 (2001): p. 49-54.
43. E.A. Trillo, L.E. Murr, *J. Mater. Sci.* 33, 5 (1998): p. 1263-1271.
44. E. Almanza, L.E. Murr, *J. Mater. Sci.* 35, 13 (2000): p. 3181-3188.
45. A. Pardo, M. Merino, A. Coy, F. Viejo, M. Carboneras, R. Arrabal, *Acta Mater.* 55, 7 (2007): p. 2239-2251.
46. R. Leiva-Garcia, M.J. Munoz-Portero, J. Garcia-Anton, *Corros. Sci.* 51, 9 (2009): p. 2080-2091.
47. S.M. Bruemmer, *Corrosion* 42, 1 (1986): p. 27-35.
48. S.M. Bruemmer, L.A. Chariot, B.W. Arey, *Corrosion* 44, 6 (1988): p. 328-333.
49. A. Lewis, M. Kilburn, I. Papageorgiou, G. Allen, C. Case, *J. Biomed. Mater. Res. A* 73, 4 (2005): p. 456-467.
50. C. Valero-Vidal, L. Casabán-Julian, I. Herraiz-Cardona, A. Igual-Muñoz, *Mater. Sci. Eng. C* 33, 8 (2013): p. 4667-4676.
51. W.C. Rodrigues, L.R. Broilo, L. Schaeffer, G. Knornschild, F.R.M. Espinoza, *Powder Technol.* 206, 3 (2011): p. 233-238.
52. E. Bettini, T. Eriksson, M. Boström, C. Leygraf, J. Pan, *Electrochim. Acta* 56, 25 (2011): p. 9413-9419.
53. S.M. Bruemmer, B.W. Arey, L.A. Charlot, *Corrosion* 48, 1 (1992): p. 42-49.
54. C. Montero-Ocampo, A. Salinas Rodriguez, *J. Biomed. Mater. Res.* 29, 4 (1995): p. 441-453.
55. S.M. Schlegel, S. Hopkins, M. Frary, *Scrip. Mater.* 61, 1 (2009): p. 88-91.
56. P. Lin, G. Palumbo, U. Erb, K.T. Aust, *Scrip. Metall. Mater.* 33, 9 (1995): p. 1387-1392.
57. P. Panigrahi, Y. Liao, M.T. Mathew, A. Fischer, M.A. Wimmer, J.J. Jacobs, L.D. Marks, *J. Biomed. Mater. Res. B* 102, 4 (2014): p. 850-859.
58. V. Randle, *Acta Mater.* 52, 14 (2004): p. 4067-4081.
59. V. Randle, *Mater. Character.* 47, 5 (2001): p. 411-416.
60. E.M. Lehockey, A.M. Brennenstuhl, I. Thompson, *Corros. Sci.* 46, 10 (2004): p. 2383-2404.
61. M. Shimada, H. Kokawa, Z.J. Wang, Y.S. Sato, I. Karibe, *Acta Mater.* 50, 9 (2002): p. 2331-2341.
62. C.S. Tedmon, D.A. Vermilye, J.H. Rosolows, *J. Electrochem. Soc.* 118, 2 (1971): p. 192-202.
63. B.W. Bennett, H.W. Pickering, *Metall. Trans. A* 18, 6 (1991): p. 1117-1124.
64. M. Povich, *Corrosion* 34, 2 (1978): p. 60-65.
65. H. Sahlaoui, K. Makhlof, H. Sidhom, J. Philibert, *Mater. Sci. Eng. A* 372, 1-2 (2004): p. 98-108.
66. P. Stemmer, R. Pourzal, Y.F. Liao, L. Marks, M. Morlock, J.J. Jacobs, M.A. Wimmer, A. Fischer, *Am. Soc. Test Mater.* 1560 (2013): p. 251-267.
67. G. Palumbo, K.T. Aust, E.M. Lehockey, U. Erb, P. Lin, *Scrip. Mater.* 38, 11 (1998): p. 1685-1690.
68. ASTM F1537-11, "Standard Specification for Wrought Cobalt-28Chromium-6Molybdenum Alloys for Surgical Implants (UNS R31537, UNS R31538, and UNS R31539)" (West Conshohocken, PA: ASTM International, 2011).
69. D. Brandon, *Acta Metall.* 14, 11 (1966): p. 1479-1484.
70. R.T. Blunt, "White Light Interferometry—A Production Worthy Technique for Measuring Surface Roughness on Semiconductor Wafers," Proceedings of CS MANTECH Conference 2006 (Beaverton, OR: CS MANTECH, 2006), p. 59-62.
71. M.K. Miller, K.F. Russell, K. Thompson, R. Alvis, D.J. Larson, *Microsc. Microanal.* 13, 6 (2007): p. 428-436.
72. R. Fournelle, J. Clark, *Metall. Trans. B*, 3, 11 (1972): p. 2757-2767.
73. M. Mehmood, B.-P. Zhang, E. Akiyama, H. Habazaki, A. Kawashima, K. Asami, K. Hashimoto, *Corros. Sci.* 40, 1 (1998): p. 1-17.
74. A.M. Lucente, J.R. Scully, *Corros. Sci.* 49, 5 (2007): p. 2351-2361.
75. W.K. Kelly, R.N. Iyer, H.W. Pickering, *J. Electrochem. Soc.* 140, 11 (1993): p. 3134-3140.
76. R. Frankenthal, H. Pickering, *J. Electrochem. Soc.* 120, 1 (1973): p. 23-26.
77. J.A. Alonso, N.H. March, *Electrons in Metals and Alloys* (San Diego, CA: Elsevier Science, 2012).
78. Y. Shibuta, S. Takamoto, T. Suzuki, *Comput. Mater. Sci.* 44, 4 (2009): p. 1025-1029.
79. K. Sangwal, *Etching of Crystals: Theory, Experiment and Application* (Amsterdam, The Netherlands: Elsevier Science, 2012).
80. U.K. Chatterjee, S.K. Bose, S.K. Roy, *Environmental Degradation of Metals*, Corrosion Technology Series/14 (New York, NY: Taylor & Francis, 2001).
81. G.C. Wood, I.G. Wright, T. Hodgkiess, D.P. Whittle, *Mater. Corros.* 21, 11 (1970): p. 900-910.
82. E.J. Martin, R. Pourzal, M.T. Mathew, K.R. Shull, *Langmuir* 29, 15 (2013): p. 4813-4822.
83. Y. Liao, R. Pourzal, M.A. Wimmer, J.J. Jacobs, A. Fischer, L.D. Marks, *Science* 334, 6063 (2011): p. 1687-1690.
84. A. Neville, J. Hesketh, A.R. Beadling, M.G. Bryant, D. Dowson, *Proc. Inst. Mech. Eng. H* 230, 5 (2016): p. 406-420.
85. M.T. Mathew, J.J. Jacobs, M.A. Wimmer, *Clin. Orthop. Relat. Res.* 470, 11 (2012): p. 3109-3117.
86. M. Wimmer, M. Mathew, M. Laurent, C. Nagelli, Y. Liao, L. Marks, R. Pourzal, A. Fischer, J. Jacobs, *Tribochemical Reactions in Metal-on-Metal Hip Joints Influence Wear and Corrosion* (West Conshohocken, PA: ASTM International, 2013), p. 18.